Research in Astronomy and Astrophysics, 25:055003 (10pp), 2025 May
https://doi.org/10.1088/1674-4527/adc85d
CSTR: 32081.14.RAA.adc85d

The Fall and Origins of the Meteoroid Tanxi

Bin Li[1,2,3,4], Zhijian Xu[1,3,4], Ye Li[1,3], Shiyong Liao[1,3], Shoucun Hu[1,3], Weibiao Hsu[1,3], and Haibin Zhao[1,3]
[1] Purple Mountain Observatory, Chinese Academy of Sciences, Nanjing 210023, China; liye@pmo.ac.cn
[2] School of Astronomy and Space Sciences, University of Science and Technology of China, Hefei 230026, China
[3] CAS Center for Excellence in Comparative Planetology, Hefei, China
Received 2024 September 26; revised 2025 March 23; accepted 2025 March 31; published 2025 May 6

Abstract

Integrating available instrumental records with meteorite analysis could build a link between meteorite chemical groups and their original parent bodies. However, such comprehensive source region-tracing studies have not been conducted for any meteorite fall events in China. On 2022 December 15 at 09:48 UT, meteoroid Tanxi was recorded by numerous cameras in populous northern Zhejiang. This event offers an opportunity to conduct the first systematic origin-tracing study for a meteorite fall event in China. The Tanxi meteorite was classified as an H6 chondrite. This meteoroid entered the atmosphere with a velocity of 13.49 km s^{-1} and a slope of 69.52°. It most likely underwent a two-stage fragmentation process, with early fragmentation under a dynamic pressure of 0.08 MPa, and main fragmentation under a dynamic pressure of 7.83 MPa. Before colliding with the Earth, the meteoroid's heliocentric orbit had a semimajor axis of 2.363 ± 0.107 au, an eccentricity of 0.584 ± 0.019 and an inclination of 2.078 ± 0.074° . A backward D_{sh} evolution result of 5000 yr shows Tanxi's orbit is most similar to a small near-Earth asteroid 2016 WV2. The source region analysis of the Tanxi fall indicates that the H chondrites could originate from two distinct reservoirs: the 3:1J mean motion resonance complex (51.2 ± 3.7%) and the $\nu 6$ secular resonance region (41.6 ± 2.9%).

Key words: meteorites, meteors, meteoroids – celestial mechanics – planets and satellites: composition

1. Introduction

As meteoroids enter Earth's atmosphere, they break up into fragments and fall as meteorites (Brown et al. 2000; Jenniskens et al. 2012; Borovička et al. 2013). These events provide great opportunities to investigate the meteoroids' atmospheric trajectory and pre-atmospheric heliocentric orbit, which could build a link between meteorite groups with specific compositions and their original parent bodies (Spurný et al. 2017; Brown et al. 2019; Devillepoix et al. 2022). H chondrites are one of the most abundant meteorite types, representing about one third of all meteorites (Meteoritical Bulletin Database, 2024; https://www.lpi.usra.edu/meteor/metbull.php). The main belt source region of H chondrites, however, remains uncertain, with potential origins ranging from Hungaria to Jupiter–Family–Comet (JFC) region (Brown et al. 2011, 2019; Trigo-Rodríguez et al. 2015; Shober et al. 2022). Thus, collecting meteorites and analyzing the available instrumental data from these fall events could provide crucial insights into the origin and dynamic behaviors of the meteoroids.

Despite sporadic reports of meteorite falls and fireball events in China, no comprehensive source region-tracing studies-those combining meteorite analysis with instrumental records-have been conducted for any of these events. On one hand, many meteoroids do not leave any recognizable meteorite fragments on the ground, even though their entry processes were meticulously documented by satellites or video recordings (e.g., Songyuan fireball event, Dang et al. 2021). On the other hand, recent meteorite falls have predominantly occurred in remote regions of China (e.g., Banma meteorite in Qinghai Province and Longde meteorite in Ningxia Province; Meteoritical Bulletin Database, 2024). While meteorite fragments from these events have been collected and analyzed, the lack of available video records has precluded the calculation of heliocentric orbits and the reconstruction of their orbital evolution histories.

On the evening of Thursday, 2022 December 15, the sky was rather clear in northern Zhejiang Province, China. At 9:48 UT (05:48 P.M. local time), a bright fireball was witnessed by numerous people, as it traveled from south to north over Hangzhou and Jinhua City. The local residents of Tanxi Town, Pujiang County, Jinhua City reported a roaring thunder-like sound and a following tremor. The first three pieces were recovered immediately (1.77 kg, 0.35 kg and 0.07 kg), and ten more pieces were recovered between 2022 December 16 and 2023 January 18, ranging from 0.42 kg to 1.95 kg (Figure 1(a) and Table 1). The total mass of the documented samples is about 10.7 kg. The name "Tanxi" was approved by the nomenclature committee of the Meteoritical Society in 2023 January.

[4] Bin Li and Zhijian Xu contributed equally to this manuscript and therefore are listed as co-first authors.

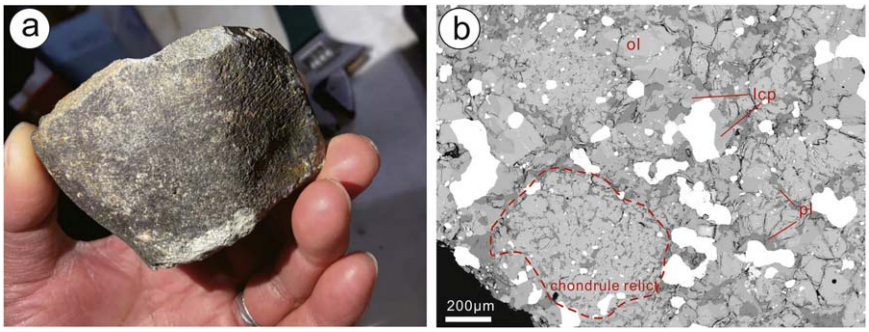

Figure 1. Photographic image (a) and BSE image (b) of Tanxi meteorite. ol = olivine, lcp = low-Ca pyroxene, pl = plagioclase.

Table 1
Overview of Recovered Tanxi Meteorites

#	Mass (g)	Latitude (°N)	Longitude (°E)
1	1950	29.633889	119.936111
2	1769	29.633056	119.932500
3	1385	29.631389	119.930556
4	981	29.631389	119.936944
5	950	29.625556	119.929444
6	760	29.631111	119.933611
7	694	29.630278	119.936944
8	552	29.630556	119.930556
9	489	29.628333	119.928611
10	471	29.625833	119.945278
11	420	29.628611	119.945278
12	350	29.626111	119.935556
13	78	29.624167	119.949722

Since the Tanxi fall event happened in areas with dense populations, it was recorded by numerous video- and photo-cameras. In this study, we integrate the available instrumental records with meteorite sample analysis. Through this approach, we estimate the atmospheric trajectory, strewn field and heliocentric orbit of the meteoroid Tanxi, trying to shed light on the origin of H chondrites. Our study provides the first comprehensive origin-tracing study for a meteorite fall event in China.

2. Data and Methods

2.1. Observation Data Sources and Data Correction

The available video recordings for astrometric analysis were provided by two amateur meteor monitoring stations at Xixing and Wuchang (Table 2). The Xixing station recorded the end of the luminous flight with a low elevation angle of about 7°, as shown by the maximum-stacked video frames in Figure 2. Even though the Wuchang station did not record the terminal parts of the luminous flight (hidden behind the mountain), it documented the late stages of the flight at a relatively high elevation angle of approximately 13°.

Table 2
Longitude, Latitude, and Altitude of the Two Meteor Monitoring Stations

Station	Lon., Lat. (°)	Alt. (m)	Field of View (H × V; °)	Sensor Resolution (H × V; pixels)	Fps
Xixing	120.2153 E 30.2199 N	95	44.3 × 88.7	1920 × 1080	25
Wuchang	120.0202 E 30.2354 N	12	44.8 × 88.2	2560 × 1440	12.5

The video was first divided into a series of single frames in which the position of the fireball could be directly measured during the unsaturated phase. The measurement for each frame was performed using a barycentric centering method, extracting the computational region as a circular area containing only the head of the fireball.

Although the fireball in the frames of both videos was heavily saturated during the rapid brightening stage (Figure 2), the "lens flare" that is caused by the reflections between lens and covered glass allowed for the measurement of these saturated areas. To obtain accurate data, the image coordinates of the "lens flare" must be converted to real coordinates. For the recordings of the Xixing station, a coordinate transformation was applied between the (x, y) position of the unsaturated real spot and that of the "lens flare". The fitting residual was found to be 0.26 pixels. The same method was also used to process the video recordings from the Wuchang station. Slightly differently, in order to facilitate the calculation of the necessary transformation relations, the "lens flare" sequence was preprocessed by image enhancement and stacking before the coordinate transformation was performed. The first and last of the "lens flare" sequence were initially aligned with the original spot, then translated in the x and y directions in steps of 0.5 pixels, and the trajectories were iteratively computed to minimize the trajectory residuals. Frames that were both saturated and had no "lens flare" for the Wuchang station were discarded because they could not be measured accurately.

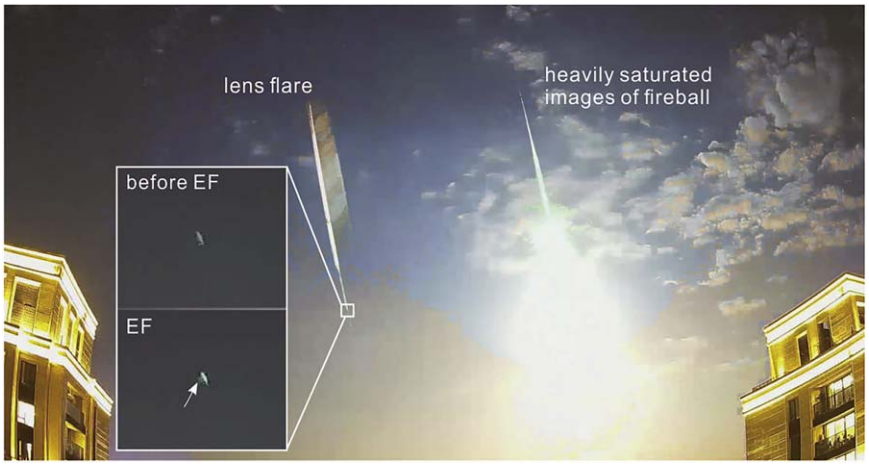

Figure 2. The max-stacked video frames of the Tanxi fireball at the Xixing station. EF refers to early fragmentation.

Table 3
Longitude, Latitude, and Altitude of the Selected Security Videos for Photometric Data

Location	Longitude (°E)	Latitude (°N)	Alt. (m)	Fps
Maodian	119.9356	29.6309	184	25
Liuxiukengkou	119.9044	29.6184	200	15
West Lake	120.1460	30.2522	10	30
Wuchang	120.0202	30.2354	12	12.5
Xixing	120.2153	30.2199	95	25

Background stars, taken by cameras from both stations one day before the event, were used for the positional calibration. The signal-to-noise ratio of the star image was improved by stacking several frames to facilitate the identification of background stars. The astrometric calibration was performed by using a third-order polynomial combined with a first-order radial term. The root mean square (rms) error in stellar astrometry was determined to be 1.6 arcmins for the Xixing station and 0.6arcmins for the Wuchang station.

The absolute time of each frame was calculated by adding the first frame time to the total time interval. At the Xixing station, the video frame rate is 25 fps, with a time interval of 0.04 s between frames. Although a few frames are occasionally dropped, the total time interval was corrected by measuring the (x, y) coordinates of the fireball in each frame. At the Wuchang station, the video frame rate is 12.5 fps, with a time interval of 0.08 s between frames. The timing from the Xixing station was treated as a "reference", and the timing offsets of Wuchang were estimated to minimize the differences in lengths along the straight line least squares (SLLS) line.

Several additional indirect video recordings of the fireball illuminating the ground and sky were used to construct the light curve (Table 3). The absolute magnitude of the light curve cannot be calibrated due to the absence of reference objects such as stars, the Moon, or the Sun in the field of view. Thus, the relative photometric changes were assessed by calculating the sum of the pixel flux of the sky. We aligned the light curve by using the brightest flares, which gave at least five matched flares with the corresponding relative time.

2.2. Calculation of Trajectory and Strewn Field

Following the intersecting plane method of Ceplecha (1987) and the line-of-sight (LoS) method of Borovička (1990), we calculated the final position $\boldsymbol{S}_{\rm f} = (S_x, S_y, S_z)$ and velocity $\boldsymbol{v}_{\rm f} = (v_x, v_y, v_z)$ of the luminous trajectory. As described by Jansen-Sturgeon et al. (2019), the Dynamic Trajectory Fit (DTF) method fitted differential equations of motion to the observations directly, which can optimize the initial solution by using the dtf_triangulation software package. Parameters for trajectory optimization include the final position $\boldsymbol{S}_{\rm f}$, the final velocity $\boldsymbol{v}_{\rm f}$, the ballistic coefficient B, the ablation coefficient σ, and the time offset between two stations Δt.

The distribution of meteorites was estimated by using the flight model of Ceplecha (1987) and Towner et al. (2022), and modified after functions in Python 3, available at www.github.com/desertfireballnetwork/DFN_darkflight. A brief description is given here.

The dynamics of meteoroid in the atmosphere is described by the following equations:

$$\frac{d\boldsymbol{v}}{dt} = -\frac{C_d A \rho_a \|v\|}{2\rho_m^{2/3} m^{1/3}}\boldsymbol{v} + \boldsymbol{a}_{\rm grav} \tag{1}$$

$$\frac{dm}{dt} = -\frac{\sigma C_d A \rho_a m^{2/3} \|v\|^3}{2\rho_m^{2/3}} \tag{2}$$

where t is the time from the start point of observation, m is the object mass, ρ_a is the atmospheric density based on the online

Density Altitude On-Line Calculators (https://wahiduddin.net/calc/density_altitude.htm), $\boldsymbol{a}_{\rm grav}$ is the gravitational acceleration of meteoroid corrected by the position under Earth centered inertial (ECI) coordinate frame, A is the shape factor (1.6, cylindrical in shape, Zhdan et al. 2007; Towner et al. 2022, ρ_m is the density of meteorites (3320 kg m^{-3}, see Section 3.1) and σ is the ablation coefficient (0.003 km^2 s^{-2}, Borovička & Kalenda 2003).

During luminous flight, $\boldsymbol{v}$ represents the velocity of the meteoroid ($\boldsymbol{v}_{\rm ECI}$, the velocity under the ECI coordinate frame) relative to that of the atmosphere ($\boldsymbol{v}_{\rm atm} = \boldsymbol{\omega}_e \times \boldsymbol{p}$, $\boldsymbol{\omega}_e$ refers to the angular velocity of the Earth, vector $\boldsymbol{p}$ represents the position of the meteoroid under the ECI coordinate frame):

$$\boldsymbol{v} = \boldsymbol{v}_{\rm ECI} - \boldsymbol{v}_{\rm atm} \tag{3}$$

During darkflight, additional horizontal velocity $\boldsymbol{v}_{\rm hori}$ (perpendicular to the meteoroid trajectory and randomly between 50 and 300 m s^{-1}) and upper wind velocity are given:

$$\boldsymbol{v} = \boldsymbol{v}_{\rm ECI} - \boldsymbol{v}_{\rm atm} + \boldsymbol{v}_{\rm hori} + \boldsymbol{v}_{\rm wind} \tag{4}$$

The upper wind data were obtained from Hangzhou Station of China Upper-Air Synoptic Station Observation (Code: CHM00058457, 70 km from the meteorite impact site) at 12 UT (data source: IGRA 2.2; https://www.ncei.noaa.gov/access/metadata/landing-page/bin/iso?id=gov.noaa.ncdc:C00975) and plotted in Figure 3.

As for drag coefficient C_d, it is a constant of 1.3 (Sansom et al. 2015) when $v > 2$ Mach and calculated based on the method of Miller & Bailey (1979) when v is between 0.3 Mach and 2.0 Mach.

2.3. Uncertainty Analysis of the Trajectory

We followed the method of uncertainty analysis used in the DFN (Desert Fireball Network) approach (Jansen-Sturgeon et al. 2020) and used the covariance matrix to estimate the uncertainty. It mainly contained the uncertainty introduced by the line-of-sight measurements and the residuals while optimizing the trajectory parameters. The measurement uncertainty was synthesized from the fireball position measurement uncertainty, the "lens flare" conversion uncertainty, and the astronomical positioning calibration residual. The measurement uncertainty was extracted in the line-of-sight of the initial fitting trajectory stage. The initial state vector and the total covariance of the trajectory were obtained by performing the SLLS. The final covariance was propagated numerically with the dynamical equation, and then the uncertainties of the trajectory parameters could be obtained.

2.4. Calculation of Heliocentric Orbit

To eliminate the effects of the Earth's strong gravitational perturbation on the orbital elements, the orbit of the meteoroid was integrated backward to a distance of five Earth Hill radii (0.05 au), using the MERCURY *N*-body hybrid integrator with the orbit of Earth and the Moon integrated separately (Chambers 1999).

2.5. Petrographic and Mineralogical Study for Recovered Meteorites

One polished thick section was prepared for the Tanxi meteorite. Petrography and mineral major chemistry analysis were performed at Purple Mountain Observatory (PMO), Chinese Academy of Sciences. A Hitachi S-3400N scanning electron microscope equipped with an energy dispersive spectroscope (EDS) was used for backscattered electron images (BSE) studies. Major elemental compositions of minerals were determined with the JEOL JXA-8230 electron microprobe by using natural and synthetic standards, and ZAF corrections (atomic number correction factor Z, absorption correction factor A, and fluorescence correction factor F). An acceleration voltage of 15 kV, a 20 nA sample current was used for silicates and chromite, and an acceleration voltage of 20 kV, a 20 nA sample current was used for metallic Fe-Ni. All phases were analyzed by using a focused electron beam and 20 s counting times per element. We adopted a pure Fe metal standard to correct for the minor overlap of the Fe-K$_\beta$ peak on the Co-K$_\alpha$ peak. The detection limits are ∼0.03 wt.% for all the elements.

3. Results and Discussion

3.1. Petrography of Tanxi Meteorite

Tanxi meteorite is highly recrystallized and composed of olivine (∼37.1 vol.%), low-Ca pyroxene (∼33.6 vol.%), high-Ca pyroxene (∼3.7 vol.%), plagioclase (∼11.4 vol.%), metallic Fe-Ni (∼9.0 vol.%), troilite (∼4.0 vol.%), chromite (∼0.7 vol.%), and Ca-phosphate (∼0.5 vol.%). Plagioclase is up to 50 μm in size. Some 0.4–1 mm sized chondrule relics are present with poorly delineated boundaries (Figure 1(b)). There is no glass present in chondrules. The degree of recrystallization of Tanxi is consistent with petrologic type 6 in the classification of Van Schmus & Wood (1967). The mineral compositions of olivine ($Fa_{18.9 \pm 0.2}$, $n = 34$), low-Ca pyroxene ($Fs_{17.0 \pm 0.3}Wo_{1.2 \pm 0.2}$, $n = 31$), and kamacite (5.9 ± 0.7 wt.% Ni and 0.50 ± 0.04 wt.% Co, $n = 14$) are characteristic of H-group chondrites (Rubin 1990; Brearley & Jones 1998). In addition, plagioclase is relatively enriched in Na ($An_{11.6 \pm 0.3}Ab_{81.6 \pm 2.3}$), and chromite is relatively depleted in Mg (Mg# = 15.6). The shock stage of Tanxi could be as low as S1 based on the sharp optical extinction of olivine and the lack of shock veins. The Archimedean method gives a bulk density of 3320 kg m^{-3}.

3.2. Trajectory and Meteorite Strewn Field

Table 4 shows measured parameters of the atmospheric trajectory from the two amateur meteor monitoring stations (Figure 4(a)). The mean spatial deviation of the atmospheric

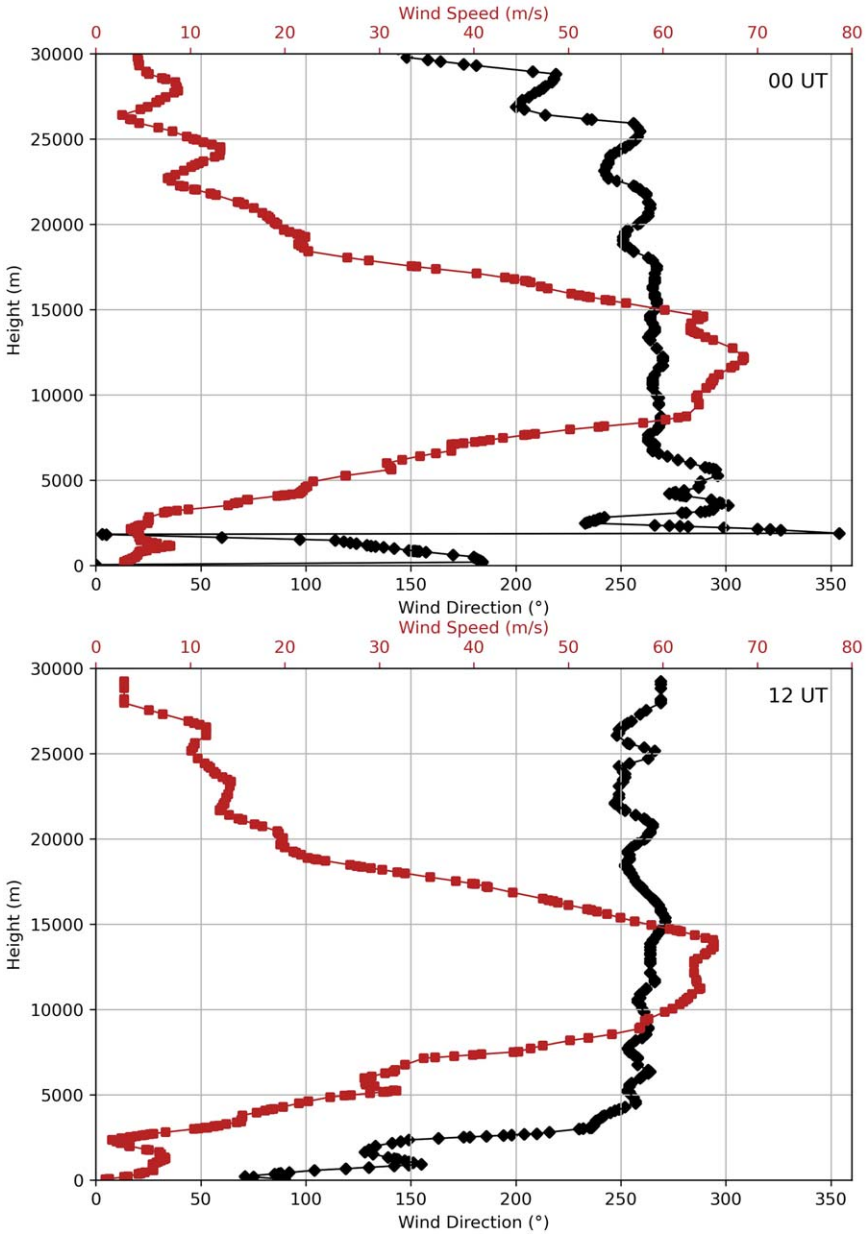

Figure 3. The vertical profile of the wind from the Hangzhou station at 00 UT and 12 UT. The wind speed was as high as 65 m s^{-1} at an altitude of 10–15 km with a westerly direction. The westerly wind continued to a height of 4.5 km, and the speed was reduced to 20 m s^{-1}. Below the altitude of 4.5 km, the average wind speed was less than 10 m s^{-1}, and the westerly wind gradually shifted to an easterly wind.

trajectory is exhibited in Figure 5. Meteoroid Tanxi began to appear at 95.42 km, and traveled from south to north, with an initial mass of 598 kg, a slope of 69.52° to the horizon, and an initial velocity of 13.49 km s^{-1}. After several flares, the main body continued to produce light until an altitude of ∼9 km with a velocity of ∼4.6 km s^{-1}.

The fragmentation process could be identified through observations and/or brightness increase in the light curve (Spurný et al. 2020, 2024; McMullan et al. 2023). The early fragmentation (EF), manifested by the video recordings (Figure 2), happened at an altitude of ∼58 km with a dynamic pressure of 0.08 MPa. We did not find the corresponding brightness increase in the light curve (Figure 6), which could be due to the relatively low signal during the early stage of luminous flight. Several brightness increases have been recorded in the light curve (from flare A to E in Figure 6). The images of the stations used to plot the light curves are shown in Figure 7. Notably, a flare event is not necessarily

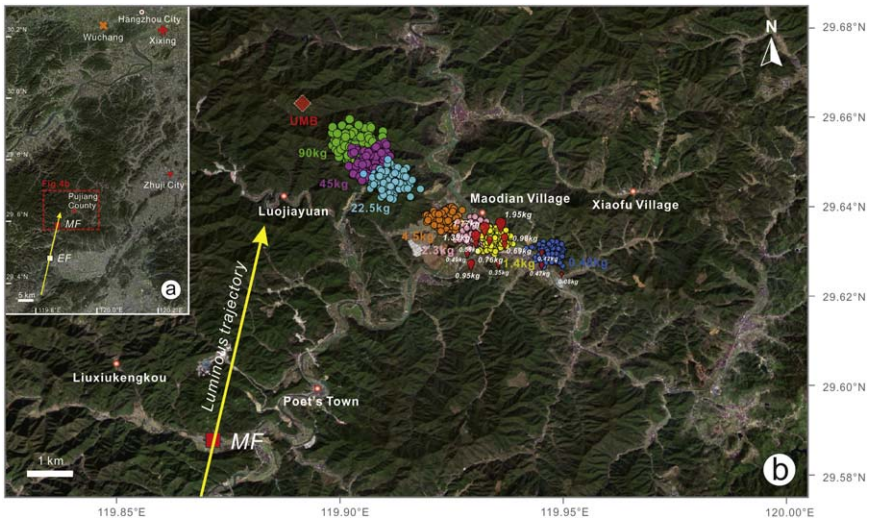

Figure 4. The map of the simulated Tanxi strewn field and the location of recovered meteorites. We assumed that meteoroid Tanxi experienced significant fragmentation during main fragmentation (MF, red square in Figure 4(a)–(b), peak E in Figure 6), and the mass loss during early fragmentation (EF, white square in Figure 4(a)) is negligible. (a) The projection of the luminous trajectory on the ground relative to Wuchang and Xixing stations. (b) The projection of the luminous trajectory on the ground relative to the simulated Tanxi strewn field, the location of recovered meteorites and the places (i.e., Maodian, Luojiayuan and Liuxiukengkou) where the photometric data were obtained. A series of fragmented masses, ranging from 20% (solid green circles), 10% (solid purple circles), 5% (solid light blue circles), 1% (solid orange circles), 0.5% (solid pink circles), 0.3% (solid yellow circles), and 0.1% (solid navy-blue circles) of the main body, were computed separately by adding a velocity perpendicular to the meteoroid trajectory (randomly between 50 and 300 m s^{-1}). The UMB symbol (unfragmented main body, solid red diamond with white dotted line) refers to the fall position for the main body without fragmentation. That is to say, any main body that has experienced main fragmentation at peak E should fall within the area between the position of UMB and fragmented mass (green circles). The source of the background image is Google Earth.

Table 4
Atmospheric Trajectory and Heliocentric Orbit Elements of the Meteoroid Tanxi

	Beginning	End	Orbital Element	
Height (km)	95.42 ± 0.17	9.03 ± 0.09	a(au)	2.363 ± 0.107
Longitude (°E)	119.8164	119.8832	e	0.584 ± 0.019
Latitude (°N)	29.359	29.6361	i(°)	2.078 ± 0.074
R.A. of Radiant (°)	344.80 ± 0.03		Peri. (°)	176.967 ± 0.103
Decl. of Radiant (°)	+9.52 ± 0.08		Node (°)	263.082 ± 0.003
V_{init}(km s^{-1})	13.49 ± 0.04		q(au)	0.98378 ± 0.00004
V_g(km s^{-1})	7.67 ± 0.07		Q(au)	3.742 ± 0.213
Slope (°)	69.52 ± 0.08		T_J	3.30 ± 0.09
Azimuth (°)	196.95 ± 0.04		…	…
Length (km)	92.27		…	…
Duration (s)	7.59		…	…

indicative of a fragmentation event; it could also result from other effects, such as the release of dust and instabilities in evaporation or erosion (Spurný et al. 2020; McMullan et al. 2023). Nevertheless, the major fragmentation is basically associated with the sharpest flare (Spurný et al. 2010; McMullan et al. 2023). According to the photometric data, we suggest that the major fragmentation (MF) is at about 28 km (i.e., flare E) under a dynamic pressure of 7.83 MPa. Previous studies found that several meteoroids record a two-stage fragmentation process, with the first stage fragmentation at relatively high altitudes (e.g., ∼45–60 km) with dynamic pressures of <0.1 MPa and the second stage fragmentation at relatively low altitudes (e.g., ∼20–30 km) with dynamic pressures of 5–0.5 MPa (e.g., meteoroid Košice and Križevci, H chondrites; Borovička et al. 2013, 2015, 2020). Fragmentation at low altitudes could even reach dynamic pressures as high as 5–7 MPa (e.g., meteoroid Hamburg, H chondrites; Brown et al. 2019). In addition, in the cases of both meteoroids Košice and Križevci, the mass loss during the fragmentation process at high altitudes is much less compared to that at low

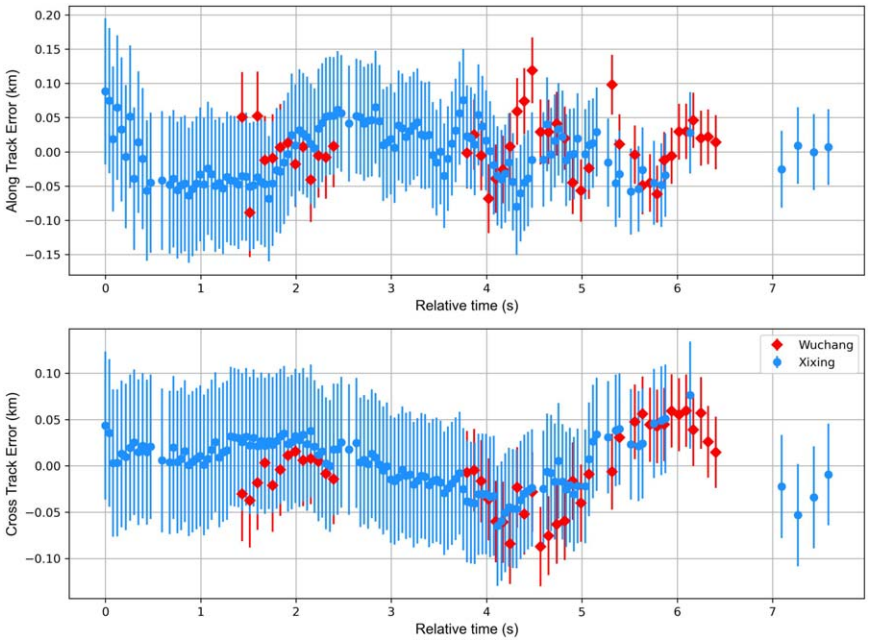

Figure 5. The mean spatial deviation of the atmospheric trajectory. The maximum value of spatial residual is about 100 m and the mean values of the along-track and cross-track residuals are below 50 m. The error bars correspond to the 1σ uncertainties on the astrometry.

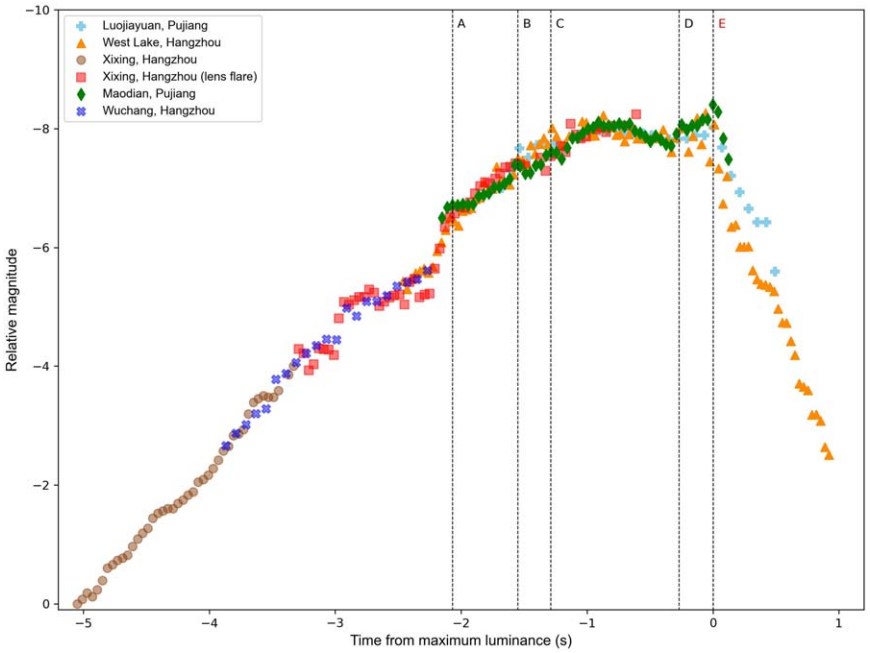

Figure 6. The relative magnitude was measured with Xixing and the other cameras were scaled to match. The light curves were aligned in time by using the brightest flares, which gave at least five matched flares with the corresponding relative time.

altitudes (Borovička et al. 2013, 2015). In this study, the dynamic pressure results for meteoroid Tanxi are basically consistent with previous findings. The first stage fragmentation is likely owed to the presence of cemented materials, and the second stage fragmentation is probably related to the presence of severe cracks (Borovička et al. 2020; Gardiol et al. 2021). It is noteworthy that the fragmentation at other altitudes cannot be entirely excluded.

Figure 7. Images of the stations used to plot the light curves. (a) West Lake, (b) Luojiayuan, (c) Maodian, (d) Wuchang. The image of Xixing is shown in Figure 2.

To check the meteorite distribution pattern, several assumptions were made as follows: (1) Meteoroid Tanxi experienced significant mass loss during MF, and the mass loss during EF is negligible. (2) A series of fragmented masses, ranging from 20% to 0.1% of the main body, were computed separately. (3) The initial velocities of the fragments were assumed to be the same as those of the main body at the time of fragmentation. (4) An additional velocity, perpendicular to the meteoroid trajectory and randomly between 50 and 300 m s^{-1}, is given.

The location of recovered meteorites is shown in Figure 4, in comparison to the simulated distribution of meteorites. The recovered meteorites are near NEE-SWW distributed, with relatively large fragments (up to 1.95 kg) on the near west side and relatively small fragments (as low as 0.078 kg) on the near east side. This distribution pattern deviated significantly from the meteoroid trajectory, most likely caused by the prevailing westerly upper wind. The simulation results show that the distribution of 0.48–2.3 kg fragments is basically comparable with that of the recovered masses, while most of the masses, including the main body and/or any fragments larger than 2.3 kg, are dispersed to the NW of the strewn field. Given that the main body fell in mountainous terrains, it is reasonable that only the fragments falling in Tanxi Town were recovered. Notably, three recovered masses are located slightly to the SW of the simulated strewn field, indicating that there could be a further fragmentation during darkflight.

3.3. Orbital Evolution History

The heliocentric orbit of Tanxi exhibits characteristics consistent with a typical Apollo-type orbit. The parameters are presented in Table 4, with a semimajor axis of 2.363 ± 0.107 au, an eccentricity of 0.584 ± 0.019, an inclination of 2.078 ± 0.074°, and a Tisserand parameter with respect to Jupiter (T_J) of 3.30 ± 0.09 (Figure 8).

The orbits of 184 near-Earth asteroids similar to the fireball, as defined by the D_{sh}-criteria of $D_{sh} \leqslant 0.15$ (Southworth & Hawkins 1963), were obtained through a search of the Minor Planet Center (MPC) asteroid database (as of 2024 April 15). A 5000 yr backward integration was performed using the MERCURY code to trace back the evolution of the D_{sh} values.

However, our dynamical analysis indicates that only 19 asteroids maintained D_{sh} values below the 0.15 threshold over the entire 5000 yr period. Figure 9 shows the temporal evolution of their D_{sh} values, which display complex oscillatory patterns due to Jupiter's gravitational perturbations. This could be due to their large aphelion distances that extend into the outer planetary region. Although asteroid 2016 WV2 has the lowest mean D_{sh} value among these objects (with the orbital configuration shown in Figure 8), the difference with the other 18 asteroids is not significant. Furthermore, as noted by Hlobik & Tóth (2024), more asteroids could be discovered with lower D_{sh} as the number of discovered asteroids increases. Notably, asteroid 2022 YO3 currently has the lowest D_{sh} value (0.031) with respect to Tanxi. Coincidentally, it had a close encounter with the Earth on 2022 December 15, at 05:20 UT, at a distance of 0.0082 au. Nevertheless, it is highly unlikely that it has a dynamical connection with Tanxi, since its D_{sh} values quickly exceeded 0.15 several hundred years ago, as observed in Figure 9. Therefore, based solely on the dynamical analysis, we are currently unable to determine definitive orbital connections between Tanxi and near-Earth asteroids. We believe that integrating physical characteristics, such as spectral features, is crucial for establishing a reliable association between Tanxi and its potential asteroid parent body.

To better understand the source region of H chondrites, we employed seven escape route models proposed by Granvik et al. (2018). Our analysis reveals that Tanxi has a 51.2 ± 3.7% probability of originating from the 3:1J mean motion resonance

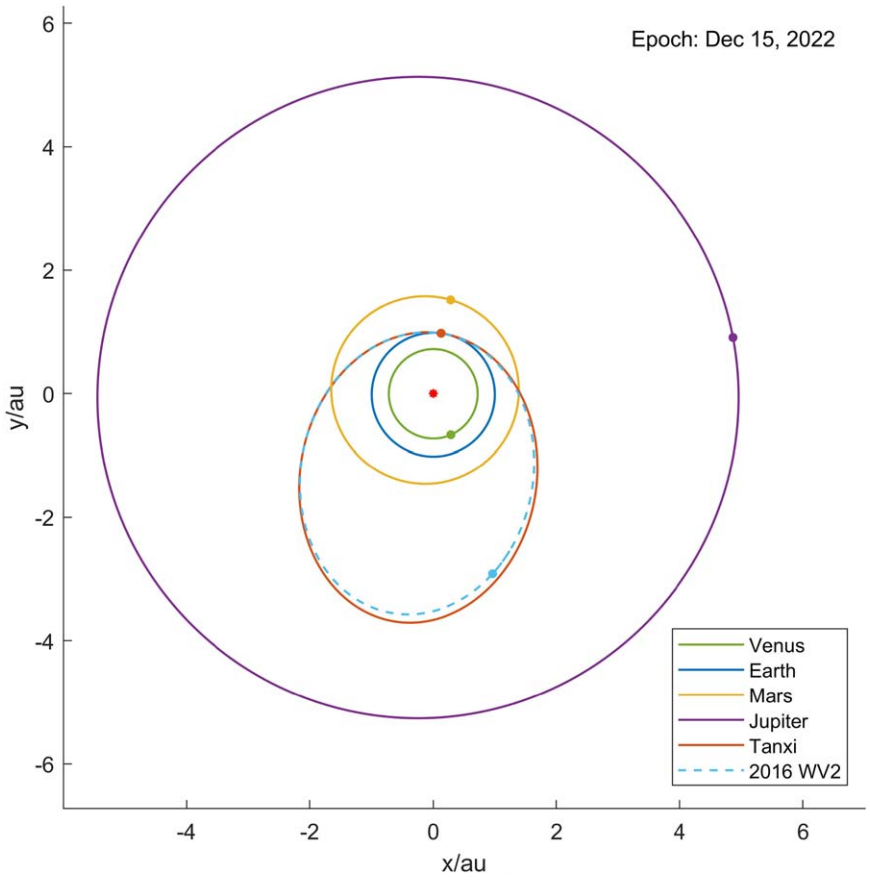

Figure 8. The orbit diagram of Tanxi and asteroid 2016 WV2.

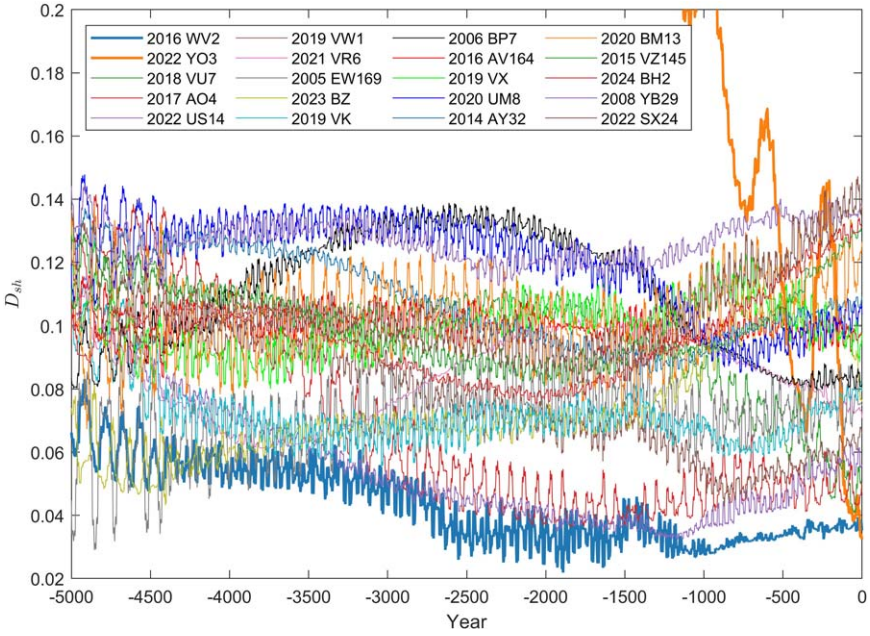

Figure 9. Backward evolution of $D_{\rm sh}$ values for 19 near-Earth asteroids that consistently maintained $D_{\rm sh}$ values below 0.15 over 5000 yr period. The result for 2022 YO3, which currently exhibits the lowest $D_{\rm sh}$ value, is also presented. The results for 2016 WV2 and 2022 YO3 are highlighted in bold for emphasis.

(MMR) complex, a 41.6 ± 2.9% likelihood of originating from the $\nu 6$ secular resonance region, a 5.2 ± 0.3% likelihood of originating from the JFC group, and a 2.0 ± 0.1% likelihood of originating from the Hungaria group. Notably, Tanxi's relatively high semimajor axis (close to 2.5 au) makes the 3:1J MMR the most probable source region, slightly surpassing the $\nu 6$ resonance in likelihood.

Ordinary chondrites, including H, L, and LL chondrites, are the most common class of meteorites (Meteoritical Bulletin Database, 2024; https://www.lpi.usra.edu/meteor/metbull.php). Previous studies showed that L and LL chondrites most likely originate from the inner edge of the main bel,t while H chondrites appear to come from a source region with a greater heliocentric distance. For instance, recent H chondrites Ejby, Arpu Kuilpu, and Hamburg appear more likely to have originated from 3:1J MMR or JFC (Spurný et al. 2017; Brown et al. 2019; Shober et al. 2022), though studies of a few H chondrites, like Annama, suggested that the inner edge of the main belt is also a potential source region for H chondrites (Trigo-Rodríguez et al. 2015). However, the source region analysis of Tanxi indicates a bimodal dynamical origin for the H chondrites, with the 3:1J MMR complex and the $\nu 6$ secular resonance region serving as competing pathways. This dual-source framework reconciles the current understanding of H chondrites delivery mechanisms: while the $\nu 6$ resonance dominates inner main belt material transport (2.1 au), the 3:1J MMR preferentially injects outer main belt bodies (2.5 au) into Earth-crossing orbits. The residual likelihood attributed to JFC and Hungaria groups further underscores the dynamical complexity inherent to the delivery of H chondrite parent bodies. These intricate mechanisms highlight the diverse pathways through which these meteorites can reach the Earth.

4. Conclusions

In this study, we provide the first comprehensive source region-tracing study for a meteorite fall event in China. The meteoroid Tanxi entered the Earth's atmosphere with a velocity of 13.49 km s^{-1} and a steep angle of 69.52° to the horizon, resulting in an NEE-SWW trending strewn field. It most likely experienced a two-stage fragmentation, with the early fragmentation at an altitude of ∼58 km under a dynamic pressure of 0.08 MPa and the main fragmentation at about 28 km under a dynamic pressure of 7.83 MPa.

Tanxi was in a typical Apollo-type orbit. By performing backward orbit integrations over 5000 yr, we find that Tanxi's orbit is most similar to a small near-Earth asteroid 2016 WV2. However, it remains uncertain whether a reliable association exists between Tanxi and 2016 WV2. Furthermore, our source region analysis demonstrates that the H chondrites exhibit a bimodal dynamical origin, with significant likelihoods of originating from both the 3:1J MMR complex (51.2 ± 3.7%) and the $\nu 6$ secular resonance region (41.6 ± 2.9%).

Acknowledgments

We thank Xiaoran Chen, Licheng Ni, and Yuning Zhu for providing the original videos, and thank Xiang Gao and Dezhao Feng for donatingthe Tanxi meteorite. This work was supported by the National Key Research and Development Program of China (2023YFE0109900), the B-type Strategic Priority Research Program of Chinese Academy of Sciences (grant No. XDB 41000000), the National Natural Science Foundation of China (grant Nos. 42273038, 62227901, 42073060 and 12150009), Space debris and NEO research project (No. KJSP2020020204), Youth Innovation Promotion Association CAS (2023332), the Science and Technology Project of Qinghai Province (2025-ZJ-T0) and the Minor Planet Foundation of China.

References

Borovička, J. 1990, Astron. Inst. Czech, 41, 391
Borovička, J., & Kalenda, P. 2003, M&PS, 38, 1023
Borovička, J., Spurný, P., Šegon, D., et al. 2015, M&PS, 50, 1244
Borovička, J., Spurný, P., & Shrbený, L. 2020, AJ, 160, 42
Borovička, J., Tóth, J., Igaz, A., et al. 2013, M&PS, 48, 1757
Brearley, A. J., & Jones, R. H. 1998, Planetary Materials, Vol. 36 (Chantilly, VA: Mineralogical Society of America), 1
Brown, P., McCausland, P., Fries, M., et al. 2011, M&PS, 46, 339
Brown, P., Vida, D., Moser, D., et al. 2019, M&PS, 54, 2027
Brown, P. G., Hildebrand, A. R., Zolensky, M. E., et al. 2000, Sci, 290, 320
Ceplecha, Z. 1987, Astron. Inst. Czech., 38, 222
Chambers, J. E. 1999, MNRAS, 304, 793
Dang, L., Liang, S., Huang, J., & Liu, S. 2021, Space Debris Research, 21, 62
Devillepoix, H. A., Sansom, E. K., Shober, P., et al. 2022, M&PS, 57, 1328
Gardiol, D., Barghini, D., Buzzoni, A., et al. 2021, MNRAS, 501, 1215
Granvik, M., Morbidelli, A., Jedicke, R., et al. 2018, Icar, 312, 181
Hlobik, F., & Tóth, J. 2024, P&SS, 240, 105827
Jansen-Sturgeon, T., Sansom, E. K., & Bland, P. A. 2019, M&PS, 54, 2149
Jansen-Sturgeon, T., Sansom, E. K., Devillepoix, H. A., et al. 2020, AJ, 160, 190
Jenniskens, P., Fries, M. D., Yin, Q.-Z., et al. 2012, Sci, 338, 1583
McMullan, S., Vida, D., Devillepoix, H., et al. 2023, M&PS, 59, 927
Miller, D. G., & Bailey, A. B. 1979, JFM, 93, 449
Rubin, A. E. 1990, GeCoA, 54, 1217
Sansom, E. K., Bland, P., Paxman, J., & Towner, M. 2015, M&PS, 50, 1423
Shober, P. M., Devillepoix, H. A., Sansom, E. K., et al. 2022, M&PS, 57, 1146
Southworth, R., & Hawkins, G. 1963, SCoA, 7, 261
Spurný, P., Borovička, J., Baumgarten, G., et al. 2017, P&SS, 143, 192
Spurný, P., Borovička, J., Kac, J., et al. 2010, M&PS, 45, 1392
Spurný, P., Borovička, J., & Shrbený, L. 2020, M&PS, 55, 376
Spurný, P., Borovička, J., Shrbený, L., Hankey, M., & Neubert, R. 2024, A&A, 686, A67
Towner, M., Jansen-Sturgeon, T., Cupak, M., et al. 2022, PSJ, 3, 44
Trigo-Rodríguez, J. M., Lyytinen, E., Gritsevich, M., et al. 2015, MNRAS, 449, 2119
Van Schmus, W., & Wood, J. A. 1967, GeCoA, 31, 747
Zhdan, I., Stulov, V., Stulov, P., & Turchak, L. 2007, SoSyR, 41, 505